Atomic structures and nanoscale electronic states on the surface of MgB$_2$ superconductor observed by scanning tunneling microscopy and spectroscopy

Akira Sugimoto, Yuta Yanase, and Toshikazu Ekino

Graduate School of Integrated Arts and Sciences, Hiroshima University, Higashi-Hiroshima 739–8521, Japan
E-mail: asugimoto@hiroshima-u.ac.jp

Takahiro Muranaka

Department of Engineering Science, University of Electro-Communications, Chofu, Tokyo, 182–8585, Japan

Alexander M. Gabovich

Institute of Physics of the National Academy of Sciences, 46 Nauki Ave., Kiev 03680, Ukraine

The systematic study of the nanoscale local electronic states on the MgB$_2$ surface was performed using the low-temperature scanning tunnel microscopy/spectroscopy (STM/STS). The STM topography shows the atomic image of the hexagonal lattice with the constant parameter $a' = 0.31$ nm, which is identified as mainly the Mg site occupancy. The temperature-dependent STS measurements were analyzed assuming the existence of two energy gaps. As a result, the fitting gap amplitudes $\Delta_{\text{fit}} \simeq 10.2$ meV and 4.8 meV were found at $T = 4.9$ K. The scanned conductance (dI / dV) maps in the area of 4×2 nm^2 show homogenous distributions of the gaps associated with the π-band. In addition, the conductance peaks at zero-bias voltage were observed through defined lines with lengths about ~0.8 nm, which is much smaller than the superconducting coherence length $\xi_{ab} \sim 40$ nm of MgB$_2$. The form of the zero-bias peaks looks like that in the case of the Andreev–Saint-James reflection at the tip-sample contact.

Keywords: MgB$_2$, superconducting gap, multiband superconductivity, STM, STS.

1. Introduction

The possibility of the multiple-gap superconductivity was predicted long ago [1,2] and has been observed or claimed to be observed for different classes of superconductors (SCs). For instance, multiple-gap features were declared to exist in the iron-based SCs [3–6], high-T_c Cu-based oxides [7,8], NbSe$_2$ [9], Nb$_3$Sn [10], V$_3$Si [11], PrOs$_4$Sb$_{12}$ [12], LuNi$_2$B$_2$C [13], LaPt$_2$Si$_2$ [14], OsB$_2$ [15], ZrB$_{12}$ [16], Cu$_x$TiSe$_2$ [17], Mo$_8$Ga$_{41}$ [18], Chevrel phases SnMo$_6$S$_8$ and PbMo$_6$S$_8$ [19], SrTiO$_3$ films and interfaces [20], and even the elemental metal of the first kind Pb [21]. Besides the purely scientific interest in the multiple-gap problem, the latter attracts attention of the researchers because there is a widely accepted hope that the electron-phonon interaction, re-

sponsible for the Cooper pairing, might be strengthened by the inter-band matrix elements [22,23], so that the critical temperature T_c and other critical parameters are enhanced as well. Among various candidates into multiple-gap SCs, the layered compound MgB$_2$ [24] is considered to be the most typical and promising material with the multiple gaps observed directly and indirectly [25–29]. It is also remarkable that the multiple-band (multiple-gap) material MgB$_2$ most probably exhibits s-wave symmetry of the superconducting order parameter, being in that sense a Bardeen–Cooper–Schrieffer (BCS)-like superconductor governed by the electron-phonon mechanism [30]. According to the conventional interpretation, two coexisting superconducting gaps of MgB$_2$ are associated with two electronic bands, namely, the two-dimensional σ band and three-dimen-

sional π band [26,28,31]. Thus, the two-band theory of superconductivity should describe MgB_2 well or at least satisfactorily. It can be checked by the direct comparison between the experiment and theory in deliberately disordered samples. Indeed, in a possible scenario of the two-gap superconductivity [32], the increased inter-band impurity scattering leads to the gap merging, i.e., the enhancement of the smaller gap and the reduction of the larger one, concomitant with the steep fall of T_c. The latter is large due to the inter-band electron-phonon pairing (in the adopted scenario, of course), so that the impurity hybridization of electron states from different bands (σ- and π-ones in MgB_2) mixes them into a new isotropic band in accordance with the Anderson theorem [33].

However, the experiment for the alloy $Mg_{1-x}Al_xB_2$ demonstrated quite different behavior [31,34]. Specifically, the actual T_c rapidly falls with the Al concentration, whereas the apparent two-gap tunnel and point-contact (Andreev–Saint-James [35–37]) spectra survive. Moreover, the smaller gap does not increase with x. Similar results were found in point-contact spectra of the carbon-substituted MgB_2 [38,39]. In particular, although T_c in $Mg(B_{1-x}C_x)_2$ changed from 39 K at $x = 0$ down to 22 K at $x = 0.1$, the apparent two-gap character of the spectra persisted at all dopings. Hence, we are forced to conclude that the picture, where two gaps emerge on different Fermi surface sections (in the momentum, k-space), encounters difficulties when applied even to the standard testing ground of the two-gap model [1,2]. On the other hand, there is an alternative viewpoint [40–43], which identifies the apparent two-band behavior of the MgB_2 compound and its modifications as the multiple-gap features of the nonhomogeneous samples, i.e., the gaps coexist in the coordinate, r-space. Therefore, the very character of the electrical conductivity and superconductivity becomes percolative [44]. The existence of such patchy structures in the layered materials are not new and have been found, in particular, in cuprates by scanning tunneling microscopy and spectroscopy (STM/STS) [45,46]. As for pure and alloyed MgB_2, the relatively wide gap distributions were also observed [34,38,39,47–49]. Nevertheless, in the most cases those distributions split into two groups in such a manner that they can be well approximated by the already conventional two-gap structures, so that the applicability of the viewpoint concerned to MgB_2 is not yet proved.

Anyway, in our previous break-junction tunneling spectroscopy (BJTS) measurements, we have obtained three representative gap groups: $2\Delta = 4–5$ meV, $8–14$ meV, and $18–24$ meV [50–52]. The observed tunneling spectra were well reproduced in details by the formal scheme based on the correlated two-gap model of the proximity effect [53] (taking place in the coordinate r-space), which is mathematically equivalent to that of the two-band k-space approach to superconductivity [54]. Those results indicate, in

particular, that different gaps are intimately linked to each other. The smallest gap among those indicated above is commonly observed by various methods except for the NMR technique [55], whereas the value of the middle-sized gap is consistent with the photoemission results suggesting the surface gap state [56,57]. The scanning tunneling measurements of surfaces often exhibit the single gap feature [58]. On the other hand, the largest gap feature can be described on the basis of the Gaussian gap distribution, suggesting that the two-dimensional layered crystal structures are spatially inhomogeneous and/or exhibit the gap anisotropy [40,50]. In the context of the inhomogeneity, extensive nanoscale measurements of the electronic local density of states (LDOS) in MgB_2 by the STM/STS are desirable to clarify the existence and properties of the multiple gaps found earlier by various techniques. Meanwhile, in addition to our previous investigations, other groups also carried out STM/STS studies. They have revealed the multiple gaps, and measured their temperature dependences [59,60]. Moreover, the precise LDOS investigations were made in the vicinity of the magnetic vortex core and, in particular, found a relatively large coherence length ξ_{ab} of ~ 40 nm [61].

The remaining problems are waiting for their solution. Nevertheless, there is an unsatisfactorily small number of clarifying experiments. In particular, there are few STM observations of the atomic MgB_2 surface arrangements, including a proper identification of the Mg and B layers. The atomic- and nanoscale LDOS and/or gap manifestations were underinvestigated because it is difficult to prepare clean and flat MgB_2 surface. The difficulty may be caused by the poor cleavage characteristics and easy oxidation of exposed Mg atoms. Meanwhile, the study of the surface together with the identification of its nature (Mg or B atoms) is very important. Indeed, the LDOS, containing many bands, may, in principle, generate the multiple gaps. Each of them are usually considered to be linked to the layer locations, i.e., the gap related to π-band electrons (commonly dubbed as "small" gaps) should dominate on the Mg layer, while its σ-counterpart should reveal itself if the B layer is studied by STS [27,62]. Therefore, the observed correlation between the specific atomic arrangement and measured superconducting gaps can shed light on the nature of superconductivity in the layered compound MgB_2.

In this paper, we present the precise STM/STS measurements with the sub-nanoscale resolution. Both the surface atomic images and the gap distributions are found. We succeeded in the observation of the identified Mg topmost layer. We observed the homogenous gap distributions, the gap being most probably the π-band one. The unusual local conductance (dI/dV) peaks, where I and V are the tunnel current and bias voltage, were found around the $V = 0$ at the extremely short length scales. Those peaks are discussed in terms of the Andreev–Saint-James reflection.

2. Experimental

The MgB$_2$ crystals were fabricated by a high-pressure synthesis technique. The details have already been described elsewhere [24]. The superconducting critical temperature $T_c \simeq 39$ K was determined by T-dependences of the resistivity and magnetic susceptibility. The specimens consist of the submicron-sized crystalline facets. Thus, the STM tip could produce the atomic-size images when the approaching angle was appropriate. The STM equipment used in this experiment was the upgraded commercially based system (Omicron LT-STM) [52,63,64]. The Pt/Ir tip was cleaned just prior to the measurements by the high-voltage field emission process with the Au single-crystal target. The specimens were cleaved below 77 K under the ultrahigh vacuum atmosphere of $\sim 10^{-8}$ Pa. The STM/STS observations were carried out in the temperature range 4.9–40 K using the heating system.

3. Results and discussion

Figure 1(a) shows the STM image of the in-situ cleaved MgB$_2$ single-crystal facet. The image displays the atomic structure. In order to evaluate its periodicity, the fast Fourier transformed (FFT) power spectrum of the STM image was derived as shown in Fig. 1(b). The main signals of the structure obtained in the FFT image reveal the period values of 0.264 and 0.265 nm (depicted by red circles in Fig. 1(b)). Both correspond to the Mg lattice period in the diagonal direction (~ 0.267 nm $= a' \times \sqrt{3}/2$), the typical lattice constant being $a' = 0.3086$ nm [24], as is shown in the model scheme of the ab plane (Fig. 1(c)). The horizontal signals indicated by red squares were very weak, which might be due to the drift during the scanning and/or the tilt of the sample. To compare the results with the idealized picture, the schematic model of the topmost ab plane of MgB$_2$ was superposed on the left bottom corner of
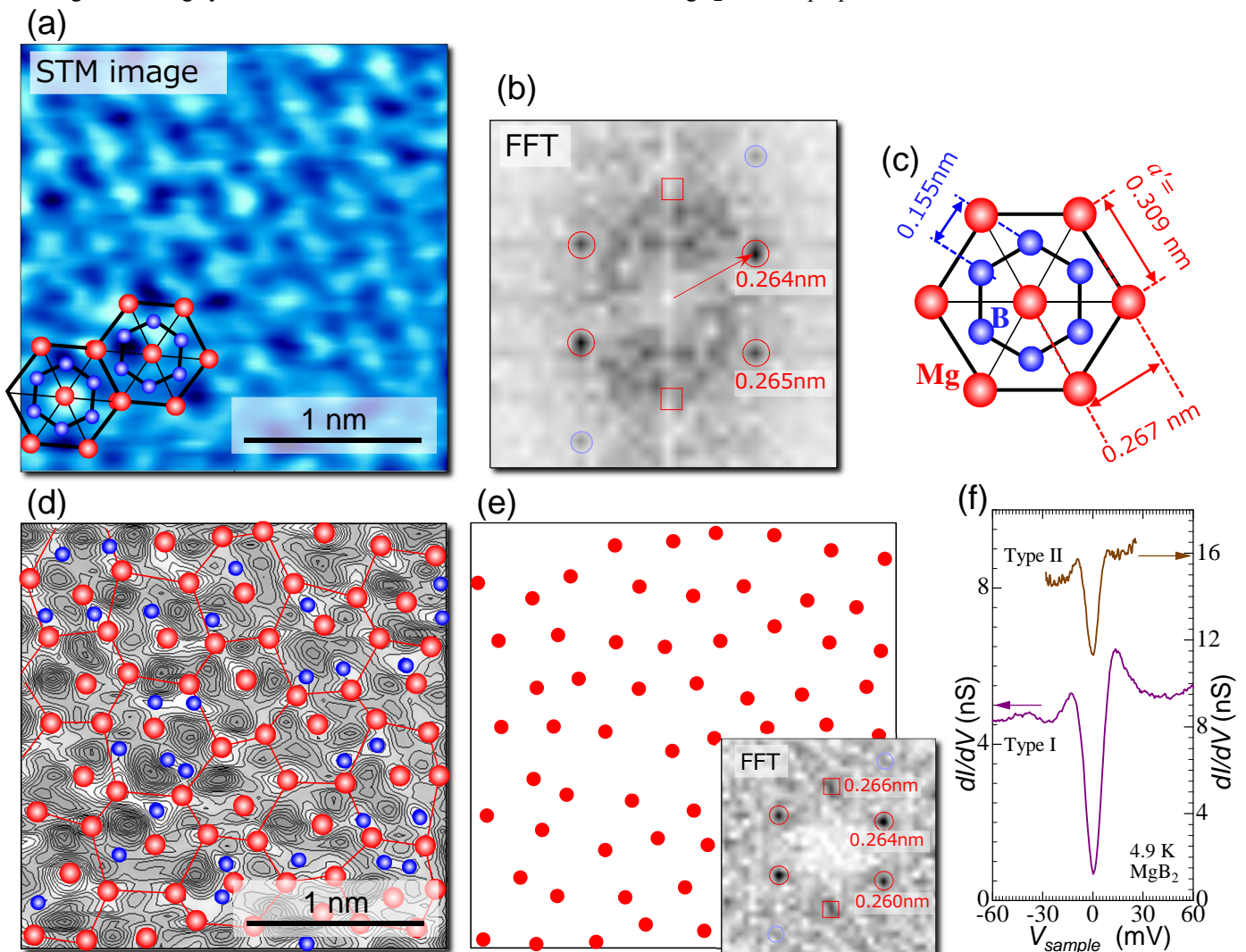

Fig. 1. (Color online) (a) The STM image (topography) of MgB$_2$ with the atomic arrangement obtained at the $T = 4.9$ K ($V = +15$ mV, $I = 0.3$ nA). (b) The fast Fourier transformed (FFT) power spectrum image of the STM image of Fig. 1(a). (c) The crystal structure of MgB$_2$ with the atomic lattice lengths. (d) The schematic draw of the atomic arrangement on the observed area together with its hexagonal structures and the STM contour plot. (e) The schematic draw of the Mg atom location (red dots) derived from Fig. 1(d), together with the FFT power spectrum image. (f) Two types of the representative conductance (dI/dV) STS spectra for MgB$_2$ obtained at $T = 4.9$ K.

Fig. 1(a) on the same scale. Those features also confirm that the observed dominant hexagonal structures are located at the Mg atom sites. To clarify the details of the atomic structure, in Fig. 1(d), the scheme of the atomic arrangement is displayed on the observed area together with its hexagonal structure and the STM contour plot. The red-ball-shaped dots (red dots) denote the positions of the major-peak atoms, which are indicated by the contour plot of the STM image. They form roughly the hexagonal structure with one central atom per one hexagon cell. Besides conventional dominant hexagonal structures, other weak irregular atomic structures were also recognized, which are depicted as the blue-ball-shaped dots (blue dots). In Fig. 1(e), the red dots from Fig. 1(d) are shown isolated. The red-dot distribution seems to be random at a glance. However, its FFT image (the inset of Fig. 1(e)) demonstrates an almost regular hexagonal pattern, which corresponds to the triangle lattice in the real space. Based on the FFT peak position, the periodic length (0.260–0.266 nm) turns out to be consistent with the Mg atomic structure (as shown in Fig. 1(c)). Therefore, it is reasonable to identify the red-dot locations with those of the Mg atoms at the topmost cleaved surface. On the contrary, the blue dots are randomly distributed and

irregularly arranged in the STM image manifesting themselves as weak peaks. It might happen that the blue-dot reflexes are due to the lower boron atom layer. However, it is difficult to detect the lower-layer signal by the STM method, so that the blue-dot random features cannot be identified with confidence.

On various facets of the cleaved surface of MgB_2 sample characterized above, we obtained by the STM/S the SC gap structures. Figure 1(f) shows two types of the representative dI/dV spectra measured at $T = 4.9$ K on different facets. Specifically, the dI/dV curves demonstrate either the peak-to-peak voltage (V_{pp}) of $\simeq 25$ mV (the "large" gap) or $\simeq 10$ mV (the "small" gap). Similar results revealing two kinds of gaps were obtained many times and are usually interpreted as the two-band two-gap structures [7]. We note that in our experiments the smaller gaps are observed more often than their larger counterparts. This trend is in accordance with the previous reports [50–52].

In order to study those gaps in more detail, we measured the T-dependences of the dI/dV curves. They are shown for large and small gaps in Figs. 2(a) and (b). The fitting curves are also depicted there as dashed lines. The fitting is based on the Dynes formula, which takes into ac-
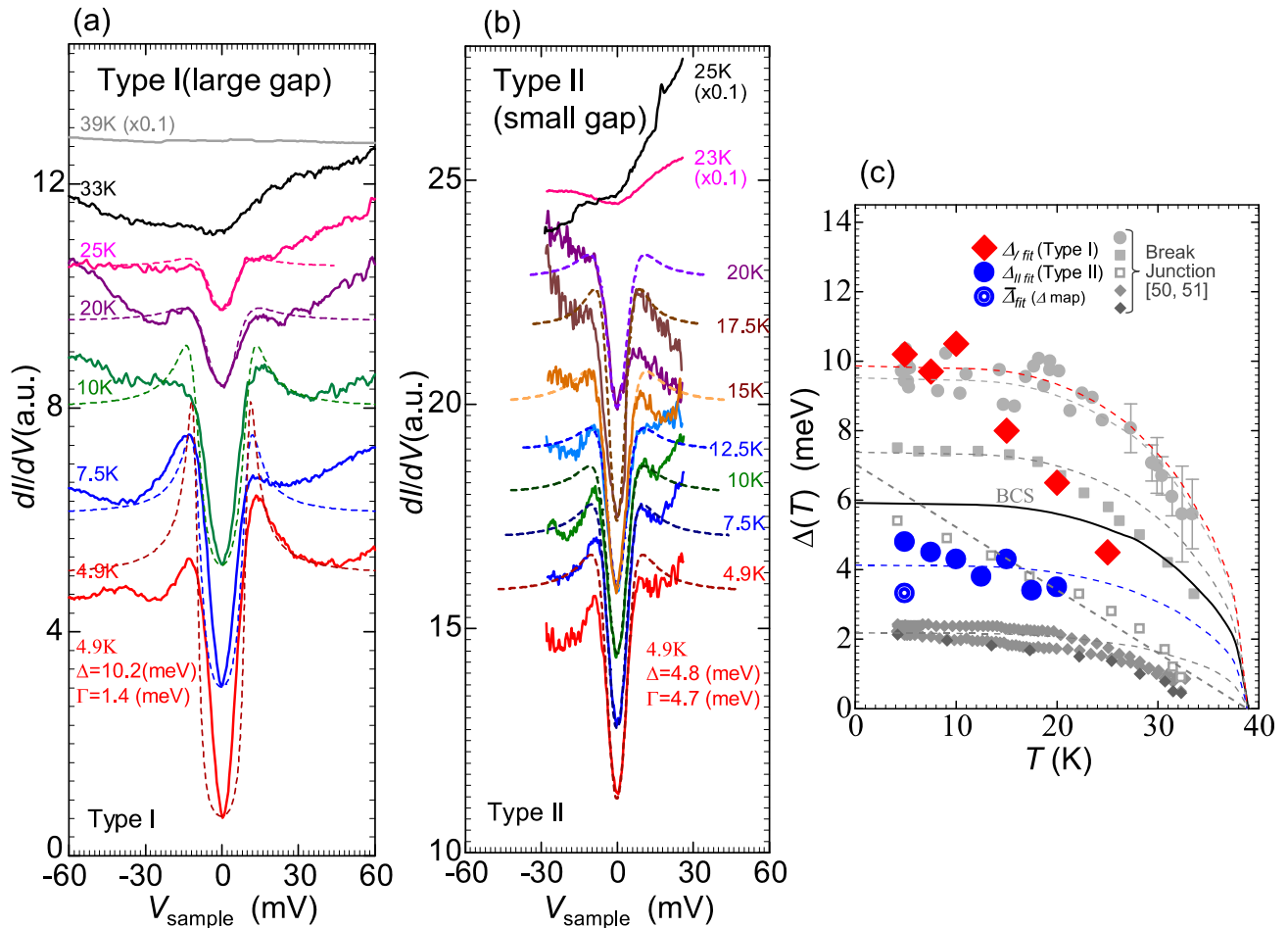

Fig. 2. (Color online) (a), (b) The T-dependences of the representative two types of dI/dV curves together with the calculated fitting curves; (a) Type I (large gap), (b) Type II (small gap). (c) The T-dependence of the fitting parameter for the gaps, $\Delta_{I\,fit}$ and $\Delta_{II\,fit}$ together with our previous data for the SIS break junction tunnel spectroscopy [50,51].

count the (phenomenological) quasiparticle lifetime broadening factor [65],

$$\frac{dI}{dV}(V) \propto \frac{d}{dV} \int_{-\infty}^{\infty} \left| \mathrm{Re} \frac{E - i\Gamma}{\sqrt{(E - i\Gamma)^2 - \Delta^2}} \right| [f(E) - f(E + eV)] dE.$$

(1)

Here $f(E)$ is the Fermi distribution function, $f(E) = [1 + \exp(E / k_B T)]^{-1}$. Γ and k_B are the broadening parameter and Boltzmann constant, respectively. The fitting gap parameter $\Delta = \Delta_{\mathrm{fit}}$ was taken as the isotropic s-wave (conventional BCS) one, in agreement with the previous experiments. The fitting quantity Δ_{fit} is smaller than that defined by the peak to peak voltage $\Delta_{pp} \equiv eV_{pp} / 2$ because of the broadening factor Γ influence. For example, in Fig. 2(a) at $T = 4.9$ K, the fitting gap parameters were $\Delta_{\mathrm{fit}} = 10.2$ meV with $\Gamma = 1.4$ meV, while Δ_{pp} is $\simeq 12$ meV. With growing temperature, the gap magnitude is reduced but the gap structure with conspicuous coherence peaks survives until $T \simeq 25$ K. At $T \geq 33$ K, the coherence peaks disappear, while the shallow depression is still observed as the remnant of the low-T gap structure. At $T = 39$ K, just below T_c, the gap-driven features completely disappear and the normal metallic behavior (the Ohm law) is restored. It should be noted that the dI / dV curves displayed in Fig. 2(a) depend on the voltage polarity. The asymmetry with respect to the V sign changes its form with T demonstrating irregular character.

In Fig. 2(b), the temperature dependence of the smaller gap is presented. The fitting procedure leads to the gap $\Delta_{\mathrm{fit}} = 4.8$ meV and broadening $\Gamma = 4.7$ meV parameters at $T = 4.9$ K. Those values are consistent with our previous BJ results of the small and middle-size gaps [50,51]. The gap concerned is much more smeared than the larger gap, i.e., the relative value of the broadening factor is much larger. The clear-cut coherent peaks were found up to $T = 20$ K and above this temperature only the depression remained, which disappeared rapidly at still higher T merging with the background.

As for the predominant gap values Δ_{fit} indicated above, they are considerably larger than other ones measured by STS [59,60]. On the other hand, they are consistent with the BJTS [31,50,51]. The origin of this discrepancy is still not known. However, we note that there exists a strict relationship between gap values in the two-band scenario, namely, the averaged gap value in the two-band s-wave SCs should possess the BCS gap-to-T_c ratio of about 3.5 [1,54]. The gap values presented here satisfy this criterion. Therefore, it seems that our STS observations reflect the bulk properties and should be considered as such.

It is remarkable that in the current STS research we observed dI / dV curves possessing either small or large gaps separately, contrary to what was found in our point contact as well as previous break junction studies [34,39,50,51].

Namely, in break junctions studies the hybrid tunnel spectra $dI / dV(V)$ simultaneously revealing both kinds of gaps (dubbed as I–II type) were observed. Those discrepancies (although not completely understood) might be due to the possible difference of the tunneling conditions for superconducting quasiparticles in both cases. Indeed, STS measurements spanning the sample surface are always the result of tunneling along one current channel determined by the tip geometry. On the other hand, the overall current across a break junction and point contact junction may include, in principle, several channels and a wide directionality cone detecting a larger surface area and different kinds of quasiparticles from various Fermi surface sections from various Fermi surface sections [66,67]. The difference in the impedance (barrier height condition) of the junction (for example, that of the break junction is of about $10 \sim 1$ kΩ, while that of the STS is of the order $\sim$ GΩ) may be also considered as the origin of the different appearance of the dI / dV curves. One of the possible origins of the "isolated" large gap (type I) is that the STS tip sometimes tends to scan in parallel to the tiny exposed ab plane facets (ab (ac) planes, for example) due to the extreme tunneling local character exhibiting the atomic resolution. Therefore, the separate large gap could be detected by the tunnel current along the ab direction, revealing the σ band corresponding to the large gap.

The temperature dependences of gaps of both types ($\Delta_{\mathrm{I\,fit}}$ and $\Delta_{\mathrm{II\,fit}}$), are plotted in Fig. 2(c), together with our previous data inferred from the SIS (superconductor–insulator–superconductor) tunnel spectroscopy data for break junctions [50,51]. One sees that both $\Delta_{\mathrm{I\,fit}}$ and $\Delta_{\mathrm{II\,fit}}$ decrease monotonically with T. However, this decrease does not obey the weak- or strong-coupling behavior inherent to s-wave BCS superconductivity. In particular, the type I gap demonstrates an extremely rapid decrease. Such a behavior might mean a suppression of superconductivity due to the proximity effect of the surface [68]. Two-band superconductivity with a certain inter-band coupling also may be responsible for the substantial deviation from the conventional mean-field behavior [54].

Figures 3(a)–(c) show typical examples of the spatial conductance dI / dV map at the bias voltages (a) $V = -15$ mV, (b) $+8$ mV, and (c) 0 mV. Although no dI / dV map shows any obvious atomic structure, inhomogeneous structures with the characteristic length of ~ 0.3 nm nm are clearly observed. Those structures almost do not change with the bias voltage V. They are usually regarded as a consequence of the difference in the surface height morphology that affects the conductance, i.e., the so-called "set point effect" [69,70]. To obtain the real electronic density of states on the surface from the dI / dV spectra, we also calculated the normalized dI / dV map by dividing the conductance dI / dV values by the value at $V = -30$ mV [$dI / dV (V) / dI / dV (V = -30$ mV)]. Thus, the set point effect is wiped out. Figures 3(d)–(f) demonstrate the normal-

Akira Sugimoto, Yuta Yanase, Toshikazu Ekino, Takahiro Muranaka, and Alexander M. Gabovich

dI/dV map

Normalized dI/dV map

(a) - 15 mV

(d) - 15 mV

1 nm

(b) +8 mV

(e) +8 mV

(c) 0 mV

(f) 0 mV

1
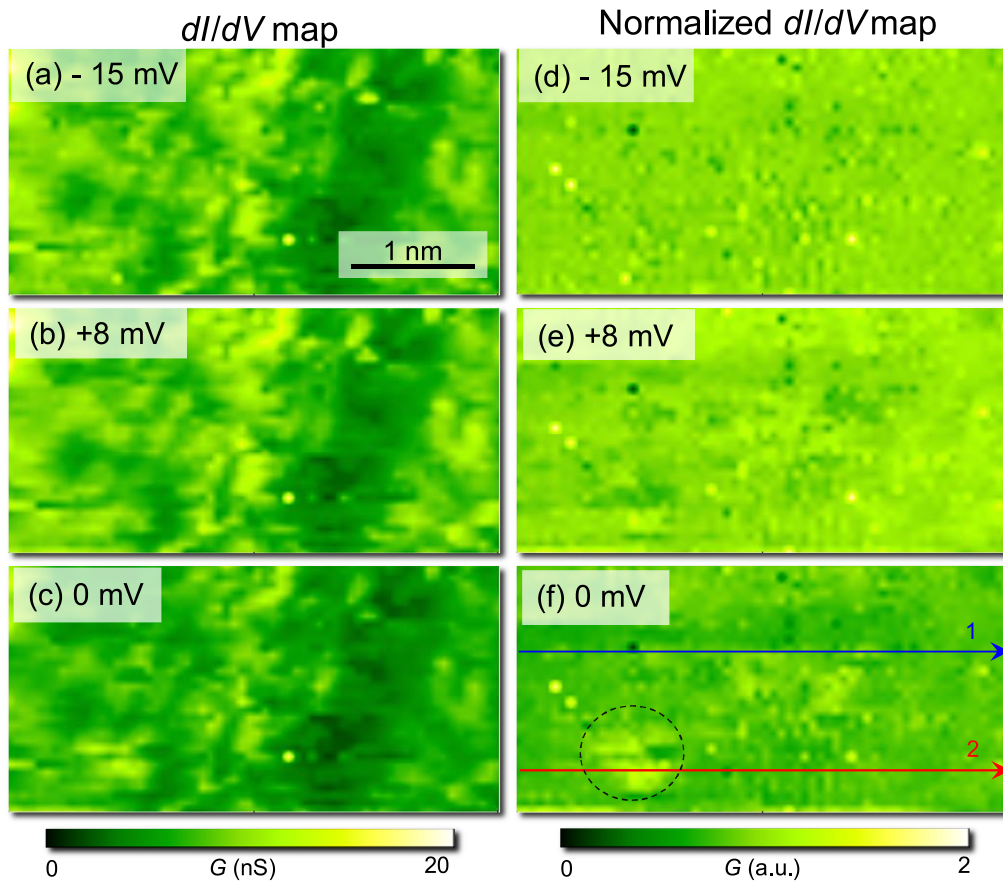
2

0   G (nS)   20   0 G (a.u.)   2

Fig. 3. (Color online) The spatial distributions of dI/dV, (dI/dV map) for the bias voltages of (a) $V = -15$ mV, (b) +8 mV, and (c) 0 mV. The normalized dI/dV map (see explanations in the text).

ized dI/dV maps thus obtained for the bias voltages of (d) $V = -15$ mV, (e) +8 mV, and (f) 0 mV. The normalized dI/dV maps are spatially quite homogeneous, reflecting the homogeneity of surface electronic structures. However, the higher-conductance island structures were still observed even after the normalization procedure. It is especially well seen in Fig. 3(f) for $V = 0$ meV (indicated by the dashed circle).

To uncover more subtle details of dI/dV spectra, including the features indicated above, we also measured the line profiles of the normalized dI/dV curve. The line profiles taken along the arrow-1 (blue) and arrow-2 (red) shown in Fig. 3(c) are presented in Fig. 4(a) and (b), respectively. In Fig. 4(a), the clear-cut gap structures continue along the profile. Furthermore, the gap spatial distribution seems to be quite homogeneous. Taking into account the gap values, the observed spectra of Fig. 4(a) reveal the type II gap, namely, the smaller one $\Delta_{pp} \sim 7$ meV. Since the Mg topmost layer is easily exposed (indeed, the Mg atomic arrangement is observed for the samples from the same batch), it is quite reasonable to suggest that the type II gaps are inherent to the whole studied area. The dominant tunnel current direction is perpendicular to the surface. Therefore, the electronic states of the three-dimensional π-band with its intrinsic small superconducting gap should generate the main part of the tunnel current

in STS measurements [27,60,62]. We also emphasize that, as has been previously mentioned while discussing Fig. 2, the value of Δ_{pp} is known to overestimate the genuine gap

Normalized dI/dV profile

(a)

(b)

4

3

2

1

0

displacement (nm)

Normalized conductance

1.6
1.4
1.2
1.0
0.8
0.6
0.4

Normalized conductance

1.6
1.4
1.2
1.0
0.8
0.6
0.4

-30 -20 -10 0 10 20 30
V_{sample} (mV)
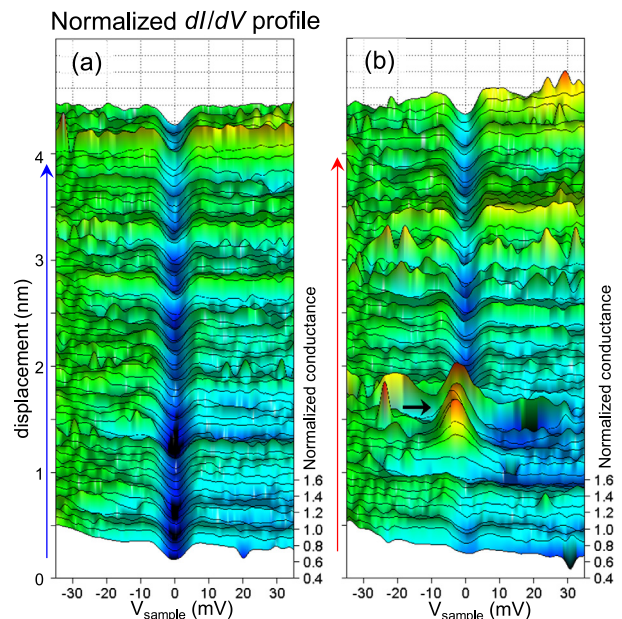
-30 -20 -10 0 10 20 30
V_{sample} (mV)

Fig. 4. (Color online) The line profiles of the dI/dV curves in the interval of ~ 0.06 nm, along (a) the arrow-1 (blue), and (b) arrow-2 (red) of Fig. 3(c).

magnitude [63]. In Fig. 4(b), additional remarkable features are observed (indicated by the black arrow). They will be examined below.

As has already been indicated, in order to obtain a "true gap" distribution map, one should take into account the "broadening effect" [65] and estimate the fitting gap values instead of the peak-to-peak distances, Δ_{pp}. However, it is very cumbersome and not realistic to employ the fitting procedure for each dI/dV curve. Therefore, we carried out the fitting for several representative experimental dI/dV curves averaged over the range of similar Δ_{pp} [63]. Figure 5(a) shows four representative experimental dI/dV curves and their fittings performed based on Eq. (1). From raw data and fitting, a linear relationship between two link-

ed quantities Δ_{fit} (meV) and Δ_{pp} (meV) was found as Δ_{fit} (meV) $\simeq 0.361\Delta_{pp} + 0.657$. It is shown in the inset of Fig. 5(b). According to this relationship, the modified gap map ($\equiv \Delta_{fit}$) was calculated. Figure 5(b) shows the histogram of the modified gap Δ_{fit}. The average of Δ_{fit} is $\overline{\Delta}_{fit} \simeq 3.3$ meV and the standard deviation is $\sigma \simeq 0.4$ meV. The Δ_{fit} map thus obtained is shown in Fig. 5(c). As comes about from the histogram, the modified gap shows almost homogeneous distribution over the observed area of a few square nanometers. We note that the peculiar patch of Fig. 4(b), indicated by the arrow, with the characteristic conductance peaks near $V \sim 0$ meV does not contain any conspicuous superconducting gap structures. That region is denoted by the white square in the gap map of Fig. 5(c).
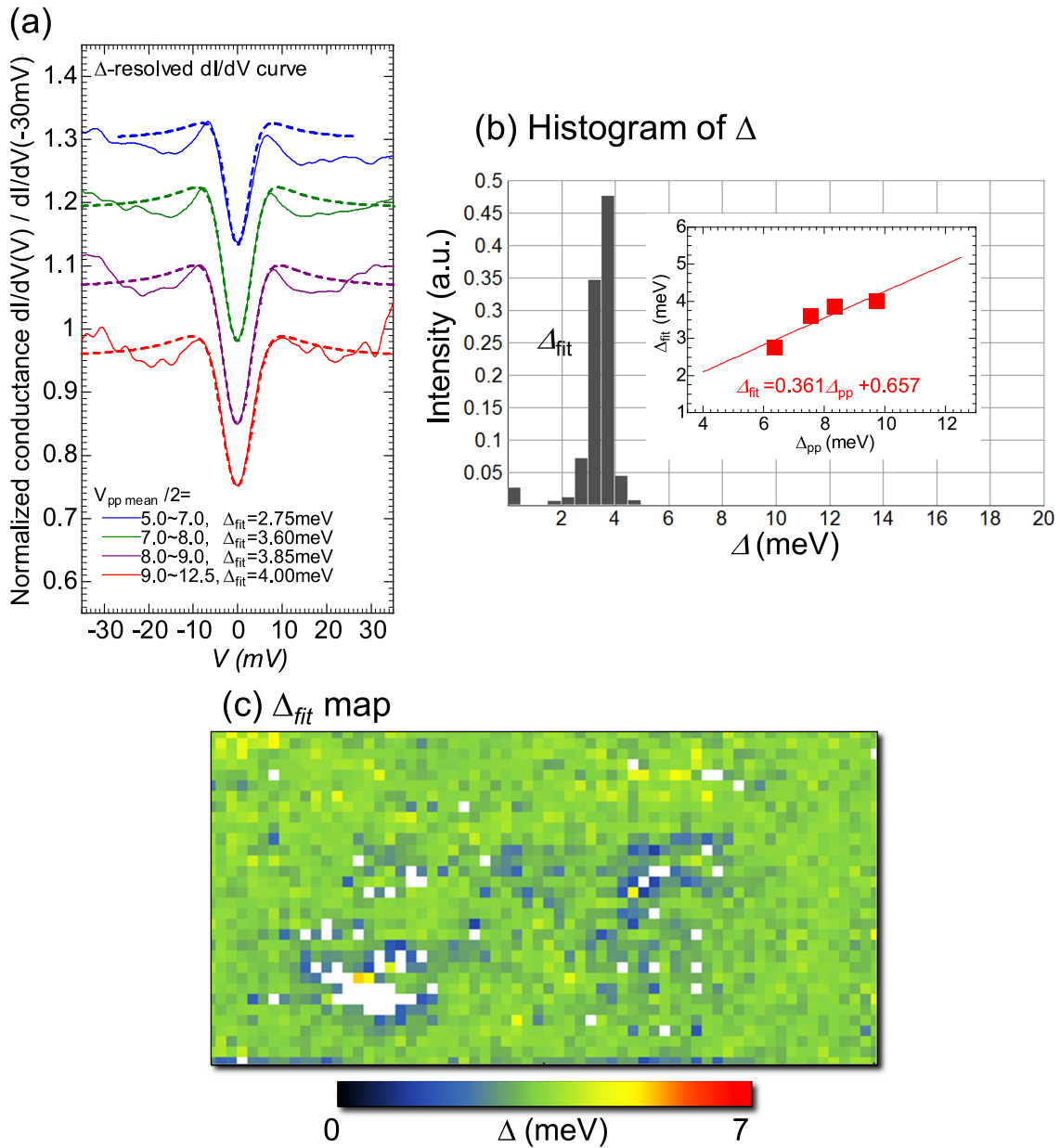

Fig. 5. (Color online) (a) The four representative experimental curves dI/dV and fitting curves based on Eq. (1). (b) The histogram of the modified gap Δ_{fit} with the non-modified data of Δ_{pp}. The inset shows the plot of the linear relationship between Δ_{fit} (meV) and Δ_{pp} (meV), $\Delta_{fit} \simeq 0.361\Delta_{pp} + 0.657$. (c) The Δ_{fit} map of the same area as in Figs. 4.

To obtain some insight into the nature of the peaks concerned, we analyzed their spatial distribution in the relevant area. In Fig. 6(a), the "zero-bias-peak height map" is shown defined as the highest value of the normalized dI/dV magnitude within the bias range of $-5\,\text{mV} < V < 5\,\text{mV}$. Then, the peculiar patch can be easily found in the left bottom corner of Fig. 6(a). Of course, the location of the patch coincides with that of the gap map [see Fig. 5(c)]. The rep-
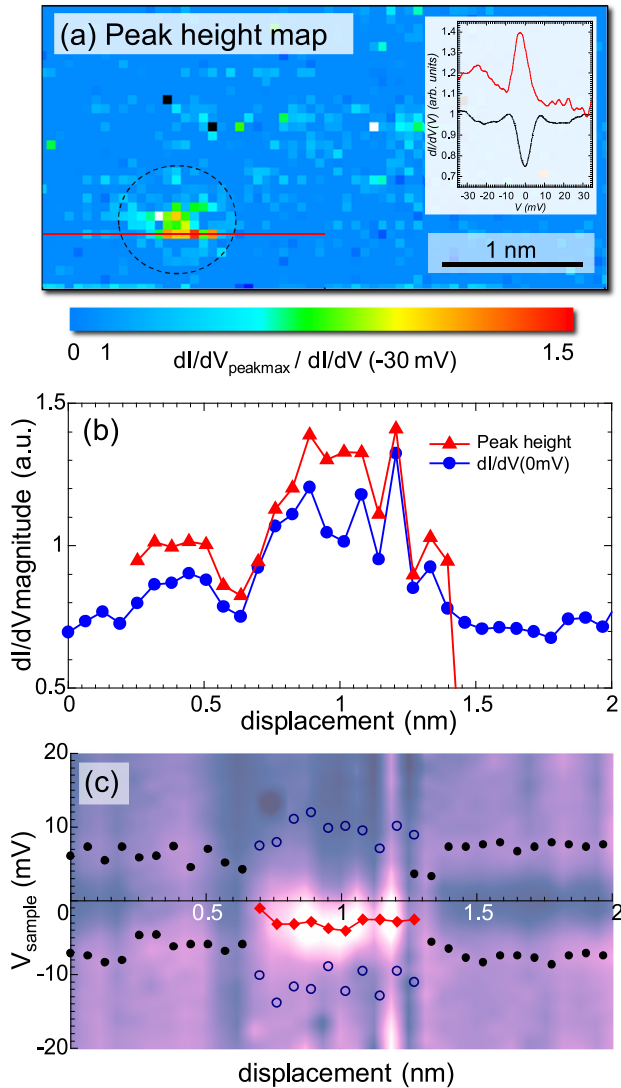

(a) Peak height map

$dI/dV_{peakmax} / dI/dV$ (-30 mV)

0   1   1.5

(b)

Peak height
dI/dV(0mV)

displacement (nm)

(c)

V_{sample} (mV)

displacement (nm)

Fig. 6. (Color online) (a) The zero-bias-peak height map. Each point is defined as the highest value of the normalized dI/dV magnitude within the bias range of $-5\,\text{mV} < V < 5\,\text{mV}$. The inset shows the representative dI/dV curve with the zero-bias-peak structure together with the dI/dV containing the superconducting quasiparticle gap (shown as black dot-dashed lines) for comparison. (b) The spatial profiles of the zero-peak height and the zero-bias dI/dV magnitude (dI/dV (x, 0 mV)) along the red line of Fig. 6(a). (c) Color-contrast image of the dI/dV profiles along the red line from (a). The data are taken from the dI/dV profile of Fig. 4(b). The superconducting gap peak and zero-bias peak positions are marked as black dots and red diamonds, respectively. The open circles depict the dip positions on the both sides of the zero-bias-peak structures.

resentative dI/dV curve with such a peaked structure is displayed in the inset of Fig. 6(a). The typical dI/dV curve involving the superconducting gap is also depicted for comparison. In the dI/dV curve, the zero-bias-peak structure is not sharp; the full width of half-maximum (FWHM) is about 8–9 mV. In Fig. 6(b), the spatial profile of the zero-bias-peak height taken along the red line of Fig. 6(a) is demonstrated. The line-cut of the zero bias dI/dV magnitude (dI/dV (x, 0 mV)) is also shown in Fig. 6(b) by blue dots. The length of the zero-bias-peak region is very short: $\sim 0.8\,\text{nm} < 1\,\text{nm}$. The color-contrast image of the conductance dI/dV profiles along the red line of Fig. 6(a) is displayed in Fig. 6(c). The superconducting gap-edge positions and the zero-bias-peak positions were marked as black dots and red diamonds, respectively. The length of the area with zero-bias peaks ($\sim 0.8\,\text{nm}$) is much shorter than the superconducting coherence length of ab surface of MgB$_2$ $\xi_{ab} \sim 40\,\text{nm}$ [61,71]. On the other hand, the former length is comparable with the atomic scale. Furthermore, as is easily recognized from Fig. 6(c), the peak positions are not located exactly at $V = 0$; the peak positions are shifted toward the negative bias direction and lie several mV below the Fermi level ($V_{peak} = -5 \dots -1\,\text{mV}$).

One might imagine several reasons of the peak emergence. For instance, it may be created at an impurity atom position, at the accidentally vortex generated in the environmental magnetic field, or the Andreev–Saint-James reflection of a certain kind. Whatever the reason invoked, the peak extremely short characteristic length has to be explained. As for the possible appearance of the vortex, it seems to be rather unrealistic because previous observations STS [58] show that the size of the vortex cores in MgB$_2$ is about 100 nm order ($\lambda \sim 100\,\text{nm}$ and $\xi_{ab} \sim 40\,\text{nm}$). Hence, it is very improbable to suggest, e.g., that the effective coherence length ξ_{local} becomes 100 times smaller at a certain spot. The impurity atom, which destroys superconductivity in its neighborhood, could, in principle, form the observed electron state. However, the large superconducting coherence length of MgB$_2$ makes this suggestion unlikely. In essence, this conclusion is the consequence of the Anderson theorem [33], which explains why the isotropic superconductivity with large coherence lengths is insensitive to local impurity-driven perturbations. The Andreev–Saint-James-like reflection might be one of the possible candidates because the FWHM of the (quasi)zero-bias-peak structure (8–9 mV) is similar to the large-gap width of this compound, $2\Delta \sim 10\,\text{meV}$ [35]. The filled and open circles in Fig. 6(c) mark positions of the superconducting gap-edge-peak and (probably) gap-related-dip on the both side of the (quasi)zero-bias-peak structures, respectively. Let us suppose for a while (although it is not an established fact) that the Andreev–Saint-James scenario is valid. Then, NS or NSNS junctions are formed between the tip and the sample in the peculiar spots instead of the nominal NIS junctions. In that hypothetical case, the dI/dV magnitude

within the gap energy region is two times larger than its counterpart outside this region [72]. Therefore, the dip position just outside the zero-bias peak could be considered as the benchmark of the superconducting gap energy. The dip are positioned at slightly larger energies ($V_{dip-dip}/2 = 7$–15 mV) than the energies ($V_{pp}/2 = 3$–7 mV) of the type II gaps; but the dip positions are rather close to the energies of the type I gaps: $V_{pp}/2 \sim 10$ mV. This might happen if the zero-bias-peak patch is a nanoscale area with an extremely low tunnel barrier (NS condition). Then, the Andreev–Saint-James-like scenario might be realized but with the tunneling quasiparticles belonging to the σ-band, i.e., demonstrating large gaps. Anyway, in the framework of the Andreev–Saint-James model, it is difficult to explain the peak shift toward the negative voltages. At least, it is not due to the experimental errors, because we always calibrated the bias voltage before the measurements. To conclude about the NS contact manifestations, we emphasize that such a boundary really seems to emerge between the tip and the small patch of the MgB_2 surface but the origin of this phenomenon remains unclear.

4. Summary

The systematic STM/STS study of the nanoscale local electronic states on the layered MgB_2 compound was carried out at low temperatures. The STM topography reveals the hexagonal atomic lattice with $a' = 0.31$ nm. We identified the observed dominant lattice structures as the Mg atoms, whereas the irregular random spots as signals from the second topmost B atoms. Two kinds of superconducting energy gaps were found by conductance dI/dV measurements. Namely, either $\Delta_{I\,fit} \simeq 10.2$ meV or $\Delta_{II\,fit} \simeq 4.8$ meV were observed while scanning the surface at $T = 4.9$ K. The gap map of the smaller type II gap was built for the area of 4×2 nm^2, showing the relatively homogenous distribution. This gap is attributed to the electronic π-band, with its average equal to $\overline{\Delta}_{fit} \simeq 3.3$ meV and the standard deviation equal to $\sigma \simeq 0.4$ meV. Besides, conductance peaks at almost zero bias voltage with no gap-edge features were observed in a local area of the linear size equal to ~ 0.8 nm. The latter results may be due to the Andreev–Saint-James reflection at NS boundaries. Namely, the peaks might originate from local low barriers formed by impurity atoms. The impurity neighborhood most probably becomes superconducting via the proximity effect.

Acknowledgment

1. H. Suhl, B.T. Matthias, and L.R. Walker, *Phys. Rev. Lett.* **3**, 552 (1959).

2. V.A. Moskalenko, *Fiz. Metallov I Metalloved.* **8**, 503 (1959) (in Russian).

3. Y. Kamihara, T. Watanabe, M. Hirano, and H. Hosono, *J. Am. Chem. Soc.* **130**, 3296 (2008).

4. K. Kuroki, S. Onari, R. Arita, H. Usui, Y. Tanaka, H. Kontani, and H. Aoki, *Phys. Rev. Lett.* **101**, 087004 (2008).

5. A. Bussmann-Holder, L. Genzel, A. Simon, and A.R. Bishop, *Zeit. Physik B* **92**, 149 (1993).

6. R.S. Gonnelli, M. Tortello, D. Daghero, G.A. Ummarino, V.A. Stepanov, and J.S. Kim, *Cent. Eur. J. Phys.* **7**, 251 (2009).

7. A. Bianconi, *J. Phys. Chem. Solids* **67**, 567 (2006).

8. Ya.G. Ponomarev, V.A. Alyoshin, E.V. Antipov, T.E. Oskina, A. Krapf, S.V. Kulbachinskii, M.G. Mikheev, M.V. Sudakova, S.N. Tchesnokov, and L.M. Fisher, *JETP Lett.* **100**, 126 (2014).

9. J.G. Rodrigo and S. Vieira, *Physica C* **404**, 306 (2004).

10. V. Guritanu, W. Goldacker, F. Bouquet, Y. Wang, R. Lortz, G. Goll, and A. Junod, *Phys. Rev. B* **70**, 184526 (2004).

11. Yu.A. Nefyodov, A.M. Shuvaev, and M.R. Trunin, *Euro. Phys. Lett.* **72**, 638 (2005).

12. G. Seyfarth, J.P. Brison, M.-A. Measson, J. Flouquet, K. Izawa, Y. Matsuda, H. Sugawara, and H. Sato, *Phys. Rev. Lett.* **95**, 107004 (2005).

13. N.L. Bobrov, S.I. Beloborod'ko, L.V. Tyutrina, V.N. Chernobay, I.K. Yanson, D.G. Naugle, and K.D.D. Rathnayaka, *Fiz. Nizk. Temp.* **32**, 641 (2006) [*Low Temp. Phys.* **32**, 489 (2006)].

14. D. Das, R. Gupta, A. Bhattacharyya, P.K. Biswas, D.T. Adroja, and Z. Hossain, *Phys. Rev. B* **97**, 184509 (2018).

15. Y. Singh, C. Martin, S.L. Bud'ko, A. Ellern, R. Prozorov, and D.C. Johnston, *Phys. Rev. B* **82**, 144532 (2010).

16. V.A. Gasparov, N.S. Sidorov, and I.I. Zver'kova, *Phys. Rev. B* **73**, 094510 (2006).

17. M. Zaberchik, K. Chashka, L. Patlgan, A. Maniv, C. Baines, P. King, and A. Kanigel, *Phys. Rev. B* **81**, 220505(R) (2010).

18. A. Sirohi, S. Saha, P. Neha, S. Das, S. Patnaik, T. Das, and G. Sheet, *Phys. Rev. B* **99**, 054503 (2019).

19. A.P. Petrovic, R. Lortz, G. Santi, C. Berthod, C. Dubois, M. Decroux, A. Demuer, A.B. Antunes, A. Pare, D. Salloum, P. Gougeon, M. Potel, and O. Fischer, *Phys. Rev. Lett.* **106**, 017003 (2011).

20. R.M. Fernandes, J.T. Haraldsen, P. Wolfle, and A.V. Balatsky, *Phys. Rev. B* **87**, 014510 (2013).

21. M. Ruby, B.W. Heinrich, J.I. Pascual, and K.J. Franke, *Phys. Rev. Lett.* **114**, 157001 (2015).

22. A.M. Gabovich and E.A. Pashitskii, *Ukr. Phys. J.* **20**, 1814 (1975).

23. N. Kristoffel, P. Konsin, and T. Ord, *Riv. Nuovo Cim.* **17**, 1 (1994).

24. J. Nagamatsu, N. Nakagawa, T. Muranaka, Y. Zenitani, and J. Akimitsu, *Nature* **410**, 63 (2001).

25. A.Y. Liu, I.I. Mazin, and J. Kortus, *Phys. Rev. Lett.* **87**, 087005 (2001).

26. D. Daghero and R.S. Gonnelli, *Supercond. Sci. Technol.* **23**, 043001 (2010).

27. H.J. Choi, D. Roundy, H. Sun, M.L. Cohen, and S.G. Louie, *Nature* **418**, 758 (2002).

28. A.A. Golubov, J. Kortus, O.V. Dolgov, O. Jepsen, Y. Kong, O.K. Andersen, B.J. Gibson, K. Ahn, and R.K. Kremer, *J. Phys.: Condens. Matter* **14**, 1353 (2002).

29. M. Putti and G. Grasso, *Mater. Res. Soc. Bull.* **36**, 608 (2011).

30. A.M. Gabovich and V.I. Kuznetsov, *Eur. J. Phys.* **34**, 371 (2013).

31. Ya.G. Ponomarev, S.A. Kuzmichev, N.M. Kadomtseva, M.G. Mikheev, M.V. Sudakova, S.N. Tchesnokov, E.G. Maksimov, S.I. Krasnosvobodtsev, L.G. Sevastyanova, K.P. Burdina, and B.M. Bulychev, *JETP Lett.* **79**, 484 (2004).

32. A.A. Golubov and I.I. Mazin, *Phys. Rev. B* **55**, 15146 (1997).

33. P.W. Anderson, *J. Phys. Chem. Solids* **11**, 26 (1959).

34. T. Klein, L. Lyard, J. Marcus, C. Marcenat, P. Szabo, Z. Hol'anova, P. Samuely, B.W. Kang, H.-J. Kim, H.-S. Lee, H.-K. Lee, and S.-I. Lee, *Phys. Rev. B* **73**, 224528 (2006).

35. A.F. Andreev, *Sov. Phys. JETP* **19**, 1228 (1964).

36. D. Saint-James, *J. de Phys.* **25**, 899 (1964).

37. G. Deutscher, *Rev. Mod. Phys.* **77**, 109 (2005).

38. Z. Hol'anova, P. Szabo, P. Samuely, R.H.T. Wilke, S.L. Bud'ko, and P.C. Canfield, *Phys. Rev. B* **70**, 064520 (2004).

39. P. Szabo, P. Samuely, Z. Pribulova, M. Angst, S. Bud'ko, P.C. Canfield, and J. Marcu, *Phys. Rev. B* **75**, 144507 (2007).

40. T. Ekino, A.M. Gabovich, M.S. Li, T. Takasaki, A.I. Voitenko, J. Akimitsu, H. Fujii, T. Muranaka, M. Pekala, and H. Szymczak, *Physica C* **426–431**, 230 (2005).

41. A.M. Gabovich, A.I. Voitenko, M.S. Li, and H. Szymczak, *Fiz. Nizk. Temp.* **28**, 1126 (2002) [*Low Temp. Phys.* **28**, 803 (2002)].

42. A.M. Gabovich, M.S. Li, M. Pekala, H. Szymczak, and A.I. Voitenko, *J. Phys.: Condens. Matter* **14**, 9621 (2002).

43. A.M. Gabovich, M.S. Li, M. Pekala, H. Szymczak, and A.I. Voitenko, *Physica C* **405**, 187 (2004).

44. P.A. Sharma, N. Hur, Y. Horibe, C.H. Chen, B.G. Kim, S. Guha, M.Z. Cieplak, and S.-W. Cheong, *Phys. Rev. Lett.* **89**, 167003 (2002).

45. S.H. Pan, J.P. O'Neal, R.L. Badzey, C. Chamon, H. Ding, J.R. Engelbrecht, Z. Wang, H. Eisaki, S. Uchida, A.K. Gupta, K.-W. Ng, E.W. Hudson, K.M. Lang, and J.C. Davis, *Nature* **413**, 282 (2001).

46. M.C. Boyer, W.D. Wise, K. Chatterjee, M. Yi, T. Kondo, T. Takeuchi, H. Ikuta, and E.W. Hudson, *Nat. Phys.* **3**, 802 (2007).

47. Yu.G. Naidyuk, I.K. Yanson, L.V. Tyutrina, N.L. Bobrov, P.N. Chubov, W.N. Kang, H.-J. Kim, E.-M. Choi, and S.-I. Lee, *JETP Lett.* **75**, 238 (2002).

48. T. Takasaki, T. Ekino, T. Muranaka, H. Fujii, and J. Akimitsu, *Physica C* **378–381**, 229 (2002).

49. Z.-Z. Li, H.-J. Tao, Y. Xuan, Z.-A. Ren, G.-C. Che, and B.-R. Zhao, *Phys. Rev. B* **66**, 064513 (2002).

50. T. Ekino, T. Takasaki, T. Muranaka, J. Akimitsu, and H. Fujii, *Phys. Rev. B* **67**, 094504 (2003).

51. T. Takasaki, T. Ekino, T. Muranaka, T. Ichikawa, H. Fujii, and J. Akimitsu, *J. Phys. Soc. Jpn.* **73**, 1902 (2004).

52. T. Ekino, T. Takasaki, R. Ribeiro, T. Muranaka, and J. Akimitsu, *J. Phys.: Conf. Ser.* **61**, 278 (2007).

53. W.L. McMillan, *Phys. Rev.* **175**, 537 (1968).

54. N. Schopohl and K. Scharnberg, *Solid State Commun.* **22**, 371 (1977).

55. H. Kotegawa, K. Ishida, Y. Kitaoka, T. Muranaka, and J. Akimitsu, *Phys. Rev. Lett.* **87**, 127001 (2001).

56. S. Souma, Y. Machida, T. Sato, T. Takahashi, H. Matsui, S.-C. Wang, H. Ding, A. Kaminski, J.C. Campuzano, S. Sasaki, and K. Kadowaki, *Nature* **423**, 65 (2003).

57. H. Uchiyama, K.M. Shen, S. Lee, A. Damascelli, D.H. Lu, D.L. Feng, Z.-X. Shen, and S. Tajima, *Phys. Rev. Lett.* **88**, 157002 (2002).

58. G. Rubio-Bollinger, H. Suderow, and S. Vieira, *Phys. Rev. Lett.* **86**, 5582 (2001).

59. M. Iavarone, G. Karapetrov, A.E. Koshelev, W.K. Kwok, G.W. Crabtree, D.G. Hinks, W.N. Kang, E.-M. Choi, H.J. Kim, H.-J. Kim, and S.I. Lee, *Phys. Rev. Lett.* **89**, 187002 (2002).

60. F. Giubileo, F. Bobba, A. Scarfato, A.M. Cucolo, A. Kohen, D. Roditchev, N.D. Zhigadlo, and J. Karpinski, *Phys. Rev. B* **76**, 024507 (2007).

61. M.R. Eskildsen, M. Kugler, S. Tanaka, J. Jun, S.M. Kazakov, J. Karpinski, and O. Fischer, *Phys. Rev. Lett.* **89**, 187003 (2002).

62. M. Iavarone, G. Karapetrov, A.E. Koshelev, W.K. Kwok, G.W. Crabtree, D.G. Hinks, W.N. Kang, E.-M. Choi, H.J. Kim, and S.I. Lee, *Supercond. Sci. Technol.* **17**, S106 (2004).

63. A. Sugimoto, K. Shohara, T. Ekino, Z. Zheng, and S. Yamanaka, *Phys. Rev. B* **85**, 144517 (2012).

64. A. Sugimoto, T. Ekino, and A.M. Gabovich, *Phys. Rev. B* **90**, 224503 (2014).

65. R.C. Dynes, V. Narayanamurti, and J.P. Garno, *Phys. Rev. Lett.* **41**, 1509 (1978).

66. T. Ekino, A.M. Gabovich, M.S. Li, H. Szymczak, and A.I. Voitenko, *J. Phys.: Condens. Matter* **29**, 505602 (2017).

67. A.M. Gabovich and A.I. Voitenko, *Fiz. Nizk. Temp.* **43**, 1471 (2017) [*Low Temp. Phys.* **43**, 1172 (2017)].

68. F. Giubileo, D. Roditchev, W. Sacks, R. Lamy, D.X. Thanh, J. Klein, S. Miraglia, D. Fruchart, J. Marcus, and Ph. Monod, *Phys. Rev. Lett.* **87**, 177008 (2001).

69. Y. Kohsaka, C. Taylor, K. Fujita, A. Schmidt, C. Lupien, T. Hanaguri, M. Azuma, M. Takano, H. Eisaki, H. Takagi, S. Uchida, and J.C. Davis, *Science* **315**, 1380 (2007).

70. A.J. Macdonald, Y.-S. Tremblay-Johnston, S. Grothe, S. Chi, P. Dosanjh, S. Johnston, and S.A. Burke, *Nanotechnol.* **27**, 414004 (2016).

71. J.C. Loudon, S. Yazdi, T. Kasama, N.D. Zhigadlo, and J. Karpinski, *Phys. Rev. B* **91**, 054505 (2015).

72. G.E. Blonder, M. Tinkham, and T.M. Klapwijk, *Phys. Rev. B* **25**, 4515 (1982).

Атомні структури та нанорозмірні електронні стани на поверхні надпровідника MgB$_2$, що спостерігаються за допомогою скануючої тунельної мікроскопії та спектроскопії

Akira Sugimoto, Yuta Yanase, Toshikazu Ekino, Takahiro Muranaka, Alexander M. Gabovich

Проведено систематичне дослідження нанорозмірних локальних електронних станів на поверхні MgB$_2$ з використанням низькотемпературної скануючої тунельної мікроскопії/спектроскопії (STM/STS). STM-топографія показує атомне зображення гексагональної решітки з постійним параметром $a' = 0{,}31$ нм, яке ідентифікується в основному як сукупність місць, зайнятих Mg. Проаналізовано залежності STM-вимірювань від температури в припущенні існування двох енергетичних щілин. В результаті отримано оцінку амплітуд щілин $\Delta_{\text{fit}} \simeq 10{,}2$ та $\simeq 4{,}8$ меВ при $T = 4{,}9$ K. Відскановані карти провідності (dI/dV) площею 4×2 нм^2 показали однорідний розподіл щілин, пов'язаних з π-зоною. Крім того, спостерігалися піки провідності при напрузі нульового зсуву через певні лінії на відстані близько 0,8 нм, що набагато менше, ніж довжина когерентності $\xi_{ab} \sim 40$ нм MgB$_2$. Форма піків нульового зсуву виглядає так, як у випадку відображення Андрєєва–Сент-Джеймса на контакті голка–зразок.

Ключові слова: надпровідність, поверхня MgB$_2$, скануюча тунельна мікроскопія/спектроскопія.

Атомные структуры и наноразмерные электронные состояния на поверхности сверхпроводника MgB$_2$, наблюдаемые с помощью сканирующей туннельной микроскопии и спектроскопии

Akira Sugimoto, Yuta Yanase, Toshikazu Ekino, Takahiro Muranaka, Alexander M. Gabovich

Проведено систематическое исследование наноразмерных локальных электронных состояний на поверхности MgB$_2$ с использованием низкотемпературной сканирующей туннельной микроскопии/спектроскопии (STM/STS). STM-топография показывает атомное изображение гексагональной решетки с постоянным параметром $a' = 0{,}31$ нм, которое идентифицируется в основном как совокупность мест, занятых Mg. Проанализированы зависимости STM-измерений от температуры в предположении существования двух энергетических щелей. В результате получена оценка амплитуд щелей $\Delta_{\text{fit}} \simeq 10{,}2$ и $\simeq 4{,}8$ мэВ при $T = 4{,}9$ K. Сканированные карты проводимости (dI/dV) площадью 4×2 нм^2 показали однородное распределение щелей, связанных с π-зоной. Кроме того, наблюдались пики проводимости при напряжении нулевого смещения через определенные линии на расстоянии около 0,8 нм, что намного меньше, чем длина когерентности $\xi_{ab} \sim 40$ нм MgB$_2$. Форма пиков нулевого смещения выглядит так, как в случае отражения Андреева–Сент-Джеймса на контакте игла–образец.

Ключевые слова: сверхпроводимость, поверхность MgB$_2$, сканирующая туннельная микроскопия/спектроскопия.